Environmental Science and Pollution Research (2024) 31:45383–45398
https://doi.org/10.1007/s11356-024-34114-y

RESEARCH ARTICLE

In situ nitrogen-doped graphene-TiO_2 nano-hybrid as an efficient photocatalyst for pollutant degradation

Hayat Khan[1,2]

Received: 7 January 2024 / Accepted: 20 June 2024 / Published online: 4 July 2024

Abstract

To solve environmental-related issues (wastewater remediation, energy conservation and air purification) caused by rapid urbanization and industrialization, synthesis of novel and modified nanostructured photocatalyst has received increasing attention in recent years. We herein report the facile synthesis of in situ nitrogen-doped chemically anchored TiO_2 with graphene through sol–gel method. The structural analysis using X-ray diffraction showed that the crystalline nitrogen-doped graphene-titanium dioxide (N-GT) nanocomposite is mainly composed of anatase with minor brookite phase. Raman spectroscopy revealed the graphene characteristic band presence at low intensity level in addition to the main bands of anatase TiO_2. X-ray photoelectron spectroscopy analysis disclosed the chemical bonding of TiO_2 with graphene via Ti–O–C linkage, also the substitution of nitrogen dopant in both TiO_2 lattice and into the skeleton of graphene nanoflakes. UV–Vis absorption spectroscopy analysis established that the modified material can efficiently absorb the longer wavelength range photons due to its narrowed band gap. The $N_{0.06}$-GT material showed the highest degradation efficiency over methylene blue (MB, ~98%) under UV and sulfamethoxazole (SMX, ~ 90.0%) under visible light irradiation. The increased activity of the composite is credited to the synergistic effect of high surface area via greater adsorption capacity, narrowed band gap via increased photon absorption, and reduced e^-/h^+ recombination via good electron acceptability of graphene nanoflakes and defect sites (Ti^{3+} and oxygen vacancy (V_o)). The ROS experiments further depict that primarily hydroxyl radicals ($OH^\bullet$) and superoxide anions ($O_2^{\bullet-}$) are responsible for the pollutant degradation in the process redox reactions. In summary, our findings specify new insight into the fabrication of this new material whose efficiency can be further tested in applications like H_2 production, CO_2 conversion to value-added products, and in energy conservation and storage.

Keywords Photocatalysis · Graphene nanoflakes · Characterization · UV–Vis · Pollutant degradation

Introduction

Photocatalysis is a surface phenomenon belonging to the advanced oxidation processes (AOPs) and is widely employed for the degradation of recalcitrant aqueous organic pollutants (Ruta et al. 2022; Yang et al. 2019). The process is initiated by photon absorption with sufficient energy equals or greater than the band gap of semiconductor photocatalyst, particularly 3.2 eV for crystalline anatase phase titanium dioxide (TiO_2). Such photon energy corresponds to a light wavelength of $\leq$ 387 nm, implying lies in the UV region which is $<$ 5% of the total energy of the solar spectrum (Sinhmar et al. 2020). Also, it is reported elsewhere that photoinduced charge carriers re-combine and vanish away in 10–100 ns compared to the time for electrons to be captured and migrated (100 ns to 1 ms) to the photocatalyst surface to take part in process redox reactions, consequently reducing the photocatalytic reactivity (Zhou et al. 2011). Therefore, limited UV photon response, easier recombination of electron–hole (e^-/h^+) pairs, and lower photocatalyst adsorption surface area are the key issues to be addressed, preventing TiO_2 commercialization for large-scale practical application in the areas of industrial waste water treatment, H_2 production by photolysis, conversion of CO_2 to value-added

---

Responsible Editor: Sami Rtimi

✉ Hayat Khan
khan@kfu.edu.sa; hayat.khan2@mail.mcgill.ca

[1] Department of Chemical Engineering, King Faisal University, P.O. Box 380, Al-Ahsa 31982, Kingdom of Saudi Arabia

[2] Department of Chemical Engineering, McGill University, Montreal, Quebec H3A 2B2, Canada

products, VOC removal and antibacterial and anticorrosion properties, medical treatment, road lightening and electric appliances, photochromic material, and energy conservation. Many efforts have devoted to TiO_2 band gap engineering, such as metal and non-metal doping, building heterojunctions (between the anatase-brookite-rutile crystalline phases or TiO_2 coupled with different semiconductors (ZnO, WO_3, SiO_2, CdS, etc.)), noble metal deposition, controlling the exposed crystal surface, self-doping (Ti^{3+} states and oxygen vacancies (V_o)), dye sensitization, surface organic modification, and combining with carbon material (activated carbon, fullerene, carbon nano-tubes, and graphene) to solve the stated photocatalyst limitations (Chen et al. 2023). Among them, anchoring of TiO_2 on mesoporous carbonaceous materials (reduced graphene oxide (r-GO), graphene oxide (GO), and graphene) is catching immense interest of researcher for enhanced photocatalytic efficiency due to their unique porous structure, adsorption capacity and acidity, and charge transfer properties. However, GO suffers from low electrical and thermal conductivity, surface random functionalization, and poor functionalization control during synthesis process, while r-GO has the demerits of hydrophobicity, workability restrains, and requires hazardous and potentially explosive reagents during synthesis (Catania et al. 2021). In comparison, graphene consists of a hexagonal honeycomb-shaped two-dimensional (2D) sp^2-hybridized carbon sheet of single-atom thickness has grabbed readers attention since 2004 due to its outstanding physical and chemical properties. Pristine graphene has a zero-band gap and has an optical transparency of 97.7%, making it an extremely transparent material. In addition, it possesses superior mechanical, thermal (~5000 W m^{-1} K^{-1}), electrical (~2000 S m^{-1}), and optical characteristics. An extensive surface chemistry applications are driven by graphene's enormous specific surface area (theoretical value of 2630 m^2 g^{-1}), rapid charge transport (~200,000 cm^2 V^{-1} s^{-1}), good interfacial contact with adsorbents and biocompatibility, and excellent chemical and environmental stability (Chang and Baek 2016; Khalid et al. 2012). As such, graphene can be considered as a model candidate for various fields including photocatalysis, gas sorption, separation, sensing, energy conversion and storage. However, it is worth mentioning that modulating graphene fundamental properties is crucial to meet the ever-growing demand for practical applications in said areas. In this regard, immobilization of TiO_2 on graphene and their doping with non-metal nitrogen is one of the most viable channels to tailor the diverse properties of both TiO_2 and the majestic graphene material. Among the non-metal nitrogen is a potential candidate for the chemical doping of carbon-based materials owing to its rich electron nature, strong valence bonds, matchable atomic size to that of carbon, and high electronegativity, which might provide a suitable position to fit in the graphene skeleton. Likewise, nitrogen substitution for oxygen atoms in TiO_2 lattice generate N 2p isolated impurity energy band near the TiO_2 valance band, thus narrowing its forbidden band gap and broadening semiconductor light absorption to the visible region. Also, nitrogen (N) atoms in N-TiO_2 retard the photoinduced e^-/h^+ pair recombination and can guise metastable centers due to their stability and low ionization potential (Divyasri et al. 2021). Moreover, the photogenerated charge carrier collection, mobility, and separation can potentially be enhanced by more robust interfacial contacts and the development of p-n heterojunctions between conjugated graphene structure and TiO_2. However, literature widely reports N-doped TiO_2 (Asahi et al. 2014; Smirniotis et al. 2018), N-doped graphene and or GO (Maouche et al. 2020; Xu et al. 2018), coupled TiO_2 with graphene and or TiO_2/GO (Khan et al. 2019; Padmanabhan et al. 2021), TiO_2 heterojunction with N-doped GO (Mou et al. 2014), and N-doped TiO_2 coupled with graphene and or with GO (Khalid et al. 2012; Tang et al. 2022), respectively. To the best of author information, literature is lacking the facile production of in situ N-doped TiO_2 (NT) coupled with N-doped pristine graphene (NG) heterojunctions, i.e., nitrogen-doped coupled titanium dioxide-graphene (N-GT) and its application in the degradation of organic pollutants present in wastewater.

In this study, sol–gel route was followed for the reproducible synthesis of N-GT heterostructures at room temperature for the subsequent goals.

(i) To produce a homogenously dispersed nitrogen chemically bonded to both titanium dioxide and graphene via the sole sol–gel technique.
(ii) To examine the physicochemical properties of the N-GT nano-hybrids and to correlate these attributes for the improved UV and visible light photocatalytic degradation of the model pollutants, i.e., methylene blue (MB, a common commercial textile dye) and sulfamethoxazole (SMX, a pharmaceutical antibiotics), respectively. The pollutants (MB and SMX) were selected based on their significant usage and discharge in water bodies. MB is highly soluble and forms stable solution with water at room temperature; it is used in textile industry for dyeing fabrics, paper, and leather; food industry, medicinally to treat vasoplegia after transplant operation, malaria, anemia, and urinary tract infection treatment and heparin neutralization (Oladoye et al. 2022). Moreover, MB is toxic, carcinogenic, and non-biodegradable; thus, it poses a major risk to public health and has a negative impact on the environment. Indeed, SMX is a famous and common medicinal antibiotic drug used for urinary tract infection, bronchitis, traveler's diarrhea, prostatitis, and as veterinary medicine. Recently

SMX is included in the World Health Organization model list of essential medicines. However, SMX possesses environmental chemical stability, which allows it to resist metabolic processes and natural degradation; e.g., SMX photolytic decomposition is very difficult and cannot be mineralized during oxidation (Chandra et al. 2021). Due to the non-biodegradable nature of the model pollutants, considerable amounts of these are often found in wastewater plant effluents and sewage treatment plants effluents, as well as in natural wastewater. Therefore, it is necessary to device ways to treat wastewater containing such sable highly soluble and emerging pollutants.

(iii) To probe the oxidizing species (H_2O_2, $O_2^{\bullet -}$, $OH^{\bullet}$, singlet oxygen (O^1), and photo-induced hole (h^+)) playing the dominant role in the photocatalytic degradation process.

(iv) Finally, to discuss the mechanism underlying the photogenerated e^-/h^+ pairs that lead to enhanced UV/Vis photocatalytic activity.

Experimental materials and methods

Materials

The chemicals titanium butoxide ($Ti(OBu)_4$), formic acid (CH_2O_2 (~ 98.0%), Fluka), and thiourea (NH_2CSNH_2 (≥ 99.0%), Merch) were bought from Sigma-Adrich. Anhydrous ethyl alcohol (C_2H_6O) was purchased from Fisher Scientific. Methylene blue hydrate ($C_{16}H_{18}C_lN_3S \geq 95\%$ pure) and sulfamethoxazole ($C_{10}H_{11}N_3O_3S$, > 99% pure) were obtained from Sigma–Aldrich. All the reagents were utilized as received without conducting any additional purification step. The provided graphene nanoflakes were fabricated from its carbon source, i.e., methane by inductively coupled thermal plasma system process, a technique developed by Ramona et al., in our research group at McGill University (Pristavita et al. 2011). The characteristics of graphene nano-flakes have a purity ratio of 2.5, near 345 $m^2\ g^{-1}$ of surface area, graphene crystallite size of 9.2 nm, and plane average length of about 42 nm. Deionized water (DI) was used throughout this research work.

Photocatalyst synthesis

The nanoparticles of pure TiO_2 and nitrogen-doped heterostructures (N-GT) were synthesized by the facile sol–gel process. As a first step, the graphene nano-flakes weighted quantity of 0.007 g were put into an appropriate volume of anhydrous ethyl alcohol (30 mL) followed by ultrasonication to produce a homogenous and well dispersed suspension. Titanium butoxide (5 mL) as titanium precursor was poured directly to the as-synthesized suspension under strong magnetic stirring. In second step, DI water in the amount of 30 mL with pH value of 3.0 was prepared by adding formic acid dropwise. In the next step, the pH 3.0 DI water was added dropwise to the suspension of titanium butoxide and graphene nano-flakes. The resulting blackish white sol solution was held on vigorous and constant magnetic stirring for additional 2 h, then aged for another 5 h at room temperature for steady gel formation and then dried in an electric oven at 85 °C for an overnight time. The solid pellets were grounded to amorphous powder using motor and pestle and then calcined in a programmable electric furnace at 500 °C for 2 h at a heating of 2 °C per minute. The same procedure was followed to prepare control TiO_2 without adding graphene nano-flakes and the dopant precursor thiourea.

The nitrogen dopant precursor (thiourea) was added in the amount of 0.01, 0.03, 0.06, and 0.09 mol. % on titanium (TiO_2) basis. The final materials were referred to as T (control TiO_2) and N_x-GT (nitrogen chemically doped TiO_2-graphene heterostructures), where x is the N dopant amount (mol. %).

Catalyst characterization

X-ray diffractograms of the prepared powders were recorded on a Phillips X'PERT diffractometer in the scanning range of $2\theta = 10–80°$ by using the monochromatic high intensity Cu Ka radiation ($\lambda = 0.15418$ nm) for crystalline and amorphous phase analysis and crystallite size. A SENTERRA confocal Raman microscope (Bruker, USA) was used to acquire the Raman spectra. The exposure period was set to 10 s, and the wavelength of the excitation laser was 532 nm. Potassium bromide (KBr) approach was used to examine the photocatalyst surface functional groups on a Bruker Tensor 27 Fourier-transform infrared (FTIR) spectrophotometer using the OPUS data collection tool (V 1.1). Degassing the sample under vacuum at 200 °C for 20 h using a Quantachrome Autosorb-1 Instrument, the N_2 adsorption and desorption isotherms at 77 K were measured to ascertain the textural characteristics of the pure and nano-hybrids. The BET (Brunauer–Emmett–Teller) method was used to determine the specific surface areas (P/P_o: 0.05–0.30, C constant: 50–200) of the samples, and the BJH (Barret, Joyner, and Halender) method was used to calculate the pore size distribution (pore diameter and pore volume). A scanning electron microscope (FESEM-JEOL JSM-7600) operating at a 10-kV voltage with a 10-keV energy range was used to examine the surface and particle morphology, and to notice the present elements in the hybrid structures, a transmission electron microscope (Phillips Technai G2 20TEM (FET, US)) functioned at 200 kV was employed to generate images of the material at various magnifications. The TEM has an attached energy dispersive X-ray (EDXA) analysis system to evaluate sample crystallinity. For band gap measurements, a Praying Mantis™ diffuse reflection (DRIFTS) accessory attached to a Carry 5000 NIR UV–Vis spectrophotometer (Varian Inc., USA) recorded diffuse reflectance spectra (DRS) in the 190–900-nm range. Potassium bromide (KBr) powder was employed as the analysis's reference. Utilizing an embedded Al Kα (1486.6 eV) X-ray source at a base pressure lower than 10^{-9} Torr, VG ESCALAB 3 Mark II X-ray photoelectron spectroscopy was utilized to examine the valency states and atomic percentages (at. %) of titanium, oxygen, carbon, and the non-metal dopant nitrogen, respectively. To determine every element, present in the sample, a high-resolution spectrum of the detected elements with a pass energy of 20 eV and a step size of 0.1 eV was recorded after a survey spectrum with a spot size of 300 µm and a step size of 1.00 eV was first recorded. The acquired data was analyzed using the VG Avantage software in accordance with standard protocol, which involves calibrating all peaks by positioning the primary C 1s peak at 285.0 eV, ascribed to adventitious carbon. Employing a coumarin (antioxidant) fluorescence probe approach, the quantity of hydroxyl radicals ($OH^{\bullet}$) on the surface of the produced hetero-structure in water under illumination was determined (Khan et al. 2019). Photoluminescence (PL) spectra of the generated highly fluorescent 7-hydroxy-coumarin at 460 nm under the excitation at 330 nm was recorded on a FluroMax-2 spectrofluorometer supplied with a xenon (Xe) lamp. Also, to study the carrier's recombination in the as-synthesized powders, PL intensity versus wavelength was recorded on the said equipment with a 420-nm excitation source of Xe lamp.

Photocatalytic activity tests

The ultraviolet (UV) photocatalytic degradation of the prepared powders was tested by analyzing the decoloration of methylene blue (MB) in a cylindrical batch reactor. Two separate flasks containing 0.1 g L^{-1} nanophotocatalyst powder and 0.006 g L^{-1} of pollutant were sonicated for 30 min to generate stabilized suspension and solution, respectively, before pouring into the cylindrical batch reactor (2.4 L operating volume). Uninterrupted and externally filtered air as oxygen source was bubbled continuously into the reactor suspension under constant magnetic stirring till the completion of the experiment. The light source for light irradiation was a UV germicidal lamp (λ_{max} of 254 nm, US Atlantic Ultraviolet Corp. GPH212T5L/4). The centrally mounted vertical lamp in the reactor was protected in a quartz sleeve. To establish the adsorption equilibrium, implying the model pollutant maximum adsorption on the photocatalyst surface, the first 40 min was performed in the dark. After that, the UV experiment was initiated by light irradiation exposure for 1 h duration; every 10 min, an aliquot of 5 mL solution was withdrawn and filtered to separate the photocatalyst particles by using Millipore syringe filters with a porosity of 0.22 µm. The residual MB concentration was analyzed on Carry 5000 NIR UV–Vis spectrophotometer by determining its absorbance maxima at 664 nm. During the activity studies, the pH was measured using a Fisher Accumet TMAB15 pH meter that came with a glass pH electrode; the reactor pH was steady in the range of 5.9–6.0.

In the visible light activity tests, a vertically inserted mercury lamp (λ_{range} (420–660 nm), 180 W Hg-medium pressure lamp (irradiance = 270 W m^{-2}) Heraeus Nobel Light, Germany) shielded by a quartz sleeve irradiated the 800 mL reactor solution for 30 minute. Any contribution from UV radiation was eliminated using a UV blocking film (UVPS, USA). Cold water was pumped through the reactor outer jacket to maintain the temperature of the reactor suspension between 25 and 30 °C. The reactor's SMX sample was extracted and filtered using 0.22 µm syringe filters at predetermined intervals of 5 min. The decline in SMX content was measured by an Agilent 1100 series high-performance liquid chromatography (HPLC) fitted with a Zorbax Eclipse C-8column (4.6 mm × 150 mm, 3.5 µm). The previously developed analysis protocol at our lab was followed (Nasuhoglu et al. 2011). The eluents include a buffer sodium dihydrogen phosphate (NaH_2PO_4, 20 mM) and acetonitrile using an eluent gradient from 30 to 50% over a period of 10 minute at a steady flow rate of 0.8 mL $minute^{-1}$. A pH of 2.8 was adjusted for the buffer solution with phosphoric acid, and a diode array detector (DAD) operating at 262 nm wavelength was used to detect the SMX.

Radical scavenger experiments

To investigate the role of radical scavengers ($OH^{\bullet}$ radicals, $O_2^{\bullet-}$ species, singlet oxygen (O^1), H_2O_2, and photogenerated holes (h^+s)) in the photocatalytic process, model pollutant degradation rates were observed in the presence of different individual sacrificial agents such as tert-butanol [V (tBuOH/H_2O = 1:20), scavenge $OH^{\bullet}$ radicals], 1,4 benzoquinone ~ > 99% (BQ = 1 mmol L^{-1}, to annihilate $O_2^{\bullet-}$ species), catalase (22 mg L^{-1} CAT, catalyzes the H_2O_2 dismutation), azide ~ 99.99% pure (N_3^- = 1 mM, consume O^1 species), and potassium iodide (KI = 10 mmol L^{-1}, scavenge photoinduced h^+), respectively. Following the stated SOP's MB residual concentration at different time interval was analyzed on UV–Vis spectrophotometer, while the decline in SMX concentration was measured with the help of HPLC analytical equipment.

Result and discussion

The crystal structure, crystallinity, and phase identification of pure TiO_2 (T) and N-GT hybrids and nitrogen-doped graphene (NG) were analyzed using X-ray diffraction (XRD) technique. The obtained diffraction patterns (Fig. 1a) illustrated the well crystalline nature of the synthesized powders. The pointed diffraction peaks of T and N-GT match well with the crystal structure of the tetragonal anatase TiO_2. The peaks at 2θ values of 25.4°, 38.0°, 48.3°, 53.6°, 55.3°, 62.8°, 67.3°, 71.5°, and 75.6° were indexed to (101), (004), (200), (105), (211), (204), (116), (200), and (215) crystal planes of anatase phase (ICDD ref. card no 21–1272). The powders also showed a minor distinct peak of brookite phase at 30.88° on the $2\theta°$ x-axis. Moreover, the N-GT spectrum indicates that the anatase TiO_2 crystal structure is intact with both graphene and the dopant thiourea, as no characteristic peak at 26.2° was observed for the carbon specie which might be due to the low content and relatively very weak diffraction intensity of graphene or impurity oxide. Also, no anatase peak shift is witnessed implying that both graphene and N dopant are dispersed uniformly in the TiO_2 crystal structure. However, doping results in improved crystallinity as witnessed from the strong and distinct peaks at 53.6°, 55.3°, 67.3°, and 71.5° compared to pure TiO_2. Figure 1 a insert shows the XRD pattern of NG powder, the $2\theta°$ x-axis peaks at 26.2°, 41.6°, 48.6°, and 72.1° stands for the (002), (100), (101), and (104) diffraction lines, which corresponds to the hexagonal symmetry of the graphene plane (Inagaki 2000). The crystallite size of the prepared powders stated in Table 1 is calculated by using the Scherrer's formula, defined as $d = K\,\lambda/\beta\,\mathrm{Cos}\theta$, where K (0.9, a value for spherical particles) is shape factor, λ (15.418 nm) is the X-ray wavelength, θ (degrees) is the Bragg's angle, and β (radians) is the full width at half maximum (FWHM). A decrease in anatase crystallite size is observed up to dopant amount of 0.6 mol. %, further increase in dopant amount results in increased crystallite size due to oversaturation, increased growth rate of crystals, and coagulation phenomena.

Raman analysis further justified the anatase tetragonal structure in T and N-GT nanohybrids by witnessing peaks at 145.3 cm^{-1} (1-E_g), 197.3 cm^{-1} (2-E_g), 396.0 cm^{-1} (B_{1g}), 517.2 cm^{-1} (A_{1g}), and 640.9 cm^{-1} (3-E_g), respectively, as shown in Fig. 1b. The main 1-E_g vibration mode in N-GT powder showed an obvious blue-shift (Fig. 1b, insert) compared to pure T implying strong interaction of dopant and graphene with TiO_2. In addition, the decrease in peak broadening signified the increase in oxygen deficiency content, which might be ascribed to the development of high

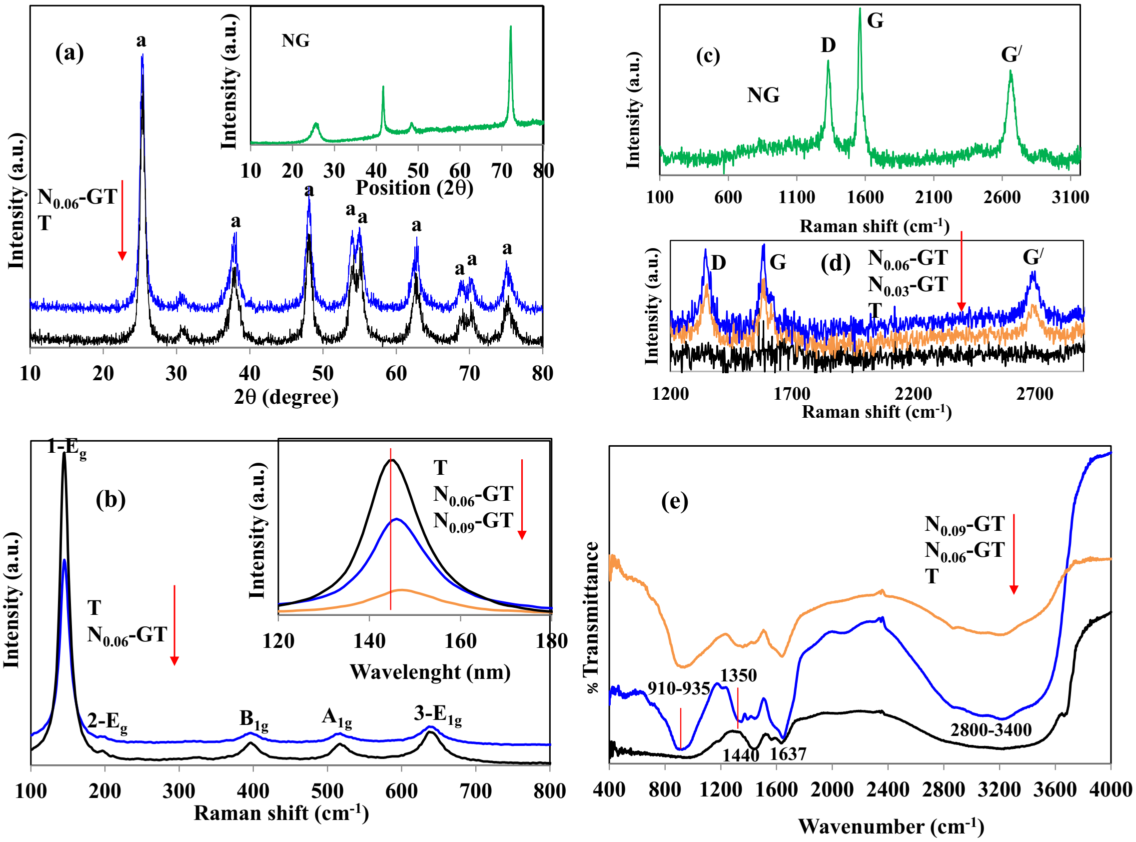

Fig. 1 **a** X-ray diffraction patterns of the representative T and $N_{0.06}$-GT — (insert) nitrogen doped graphene (NG); **b** Raman spectra of the representative T and $N_{0.06}$-GT — (insert) 1-E_g Raman band of T, $N_{0.06}$-GT, and $N_{0.09}$-GT; **c** Raman spectrum of NG; **d**, G, and G′ graphene Raman bands in $N_{0.06}$-GT, $N_{0.03}$-GT, and T; and **e** FTIR spectra of the representative $N_{0.09}$-GT, $N_{0.06}$-GT, and T, respectively. All the powder samples were calcined at 600 °C

Table 1 Physicochemical properties (crystallite size, surface area, pore size, and band gap) of the as-synthesized photocatalyst material

Photocatalyst material	Crystallite size* (nm)	BET surface area$^{\Phi}$ (m^2 g^{-1})	Pore size$^{\Psi}$ (Å)	Pore volume$^{\varphi}$ (cm^3 g^{-1})	Band gap† (eV)
T	11.0	142.533	64.0	0.307	3.10
GT	7.5	161.661	82.7	0.357	3.15
$N_{0.01}$-GT	10.0	177.304	74.2	0.340	3.00
$N_{0.03}$-GT	8.5	192.726	72.0	0.326	2.90
$N_{0.06}$-GT	7.0	220.453	68.0	0.308	2.60
$N_{0.09}$-GT	10.0	188.075	53.6	0.314	2.90

Each experiment was repeated 3–4 times

$^{\Psi}$BJH adsorption average pore width (4 V/A)

*The uncertainty in crystallite size is < 1.2 nm

$^{\Phi}$The uncertainty in surface area is 2–3 m^2 g^{-1}

$^{\varphi}$BJH adsorption cumulative volume of pore between 17.0 Å and 3000.0 Å width

†The uncertainty in bandgap is < 0.3 eV

crystallinity and N doping (Cheng et al. 2016). Raman spectrum of pure graphene is illustrated in Fig. 1c; the distinct D band at 1326.0 cm^{-1} indicative of the presence of graphene structural defects including boundaries, vacancies, bonding disorder, and heteroatoms production in graphene lattice by N doping and G band at 1564.2 cm^{-1} corresponds to the stretching of the *sp*^{2}-hybridized C = C, both peaks being characteristic of graphitic material (Sordello et al. 2014; Wen et al. 2011). Also, the peak at 2669.1 cm^{-1} signifies G′ band; its well-defined intensity reveals the presence of graphene layers with a stacking of more than five layers. Moreover, the calculated I_G/I_D ratio is greater than 2.5, implying the crystalline nature of the graphene nanoflakes (Pristavita et al. 2011). Interestingly, all the graphene Raman bands at low intensity levels were observed in the N-GT samples showing the incorporation of graphene in TiO_2 (Fig. 1d); furthermore, the D/G intensity ratio increases with N dopant amount, thereby providing convincing evidence that the dopant atoms dope into the skeleton of graphene nanoflakes (Yao et al. 2013).

The FTIR spectroscopy spectra of the synthesized powders were displayed in Fig. 1e for the examination of the surface functional groups. The strong and wide peak in the range 2860–3400 cm^{-1} matches the stretching vibration of O–H bond and N–H bond as a result of hydroxyl groups, adsorbed water molecules, and alcohol -OH groups as well the doping of amino functional groups into TiO_2 and graphene (Xu et al. 2014). The weak bands at 1637 cm^{-1} and 1440 cm^{-1} in T correspond to the bending vibration of O–H-O of the physisorbed water molecule. The peak at 1644 cm^{-1} gets much pronounced in N-GT powder illustrating stronger interaction for surface adsorbed water. The peak at 1440 cm^{-1} in T is ascribed to the C–OH stretching vibration of the alkoxy group and of Ti–O modes. The same peak is shifted to 1350 cm^{-1} in the N-GT powder attributed to the stretching vibration of C-N band (Fu et al. 2019). It was reported that the broad band from 400 to 1000 cm^{-1} region corresponds to the fingerprint of Ti–O stretch mode and bridging stretching vibration mode of Ti-O-Ti (Praveen et al. 2013). In the same region, a very strong peak appears in the range of 910–935 cm^{-1} in the N-GT powder signifying the occurrence of both Ti–O-Ti and Ti–O-C bands implying the chemical linkage of graphene with TiO_2. In summary to the FTIR analysis, it is obvious that due to dopant and graphene addition in TiO_2, the final N-GT powders had more surface adsorbed hydroxyl groups and adsorbed water molecule. Moreover, these surface hydroxyl groups may act as oxygen absorption centers to form hydroxyl radicals which played a crucial role in the photocatalytic reactions.

BET and BJH measurements were used to have the information about the specific surface area and pore size and volume of the prepared powders (Table 1). The N_2 adsorption–desorption isotherms (Fig. 1S supplementary information) curves demonstrated type-IV isotherms (typical of mesoporous materials structure) with hysteresis loop of H4 (corelated to slit-like pores) at a relative pressure range of 0.55 to 1.0 for T, while it varies from 0.4 to 1.0 for the N-GT samples, in accordance with the classification of the International Union of Pure and Applied Chemistry (IUPAC). Table 1 demonstrates that N-GT powders have higher BET surface area and pore size than control TiO_2 and graphene-TiO_2 (161.0 m^2 g^{-1}, 0.357 cm^3 g^{-1} (Khan et al. 2018)), respectively. This implies that high surface area of graphene and porosity and most important N-doping qualified to the important parameters toward the increase in photocatalyst surface area and pore size enlargement, which is beneficial for both, to facilitate the mass transport and to enhance the photocatalytic activity.

Figure 2 displays the SEM and TEM photographs of T and the representative $N_{0.6}$-GT nanoparticles. In Fig. 2a, there are many nanoparticles having spherical shape and with rough and uneven surface which principally resulted from the aggregate of nanocrystalline TiO_2. The particles get more agglomerated, acquiring ball-like structure with the addition of N dopant and graphene nanoflakes (Fig. 2b). Doped graphene with nitrogen groups could be a promising nucleation and anchor site for N-TiO_2 nanocrystals. The N-doped sites and the stronger and greater interaction between TiO_2 and graphene may be the cause of the reduced size of titania nanoparticles in the N-GT hybrid (Mou et al. 2014). The SEM micrograph of pure graphene is shown in Fig. 2Sa (supplementary information); the particles are agglomerated, overlapped with each other, and having flake like morphology. The TEM micrograph in Fig. 2c shows the encapsulation of TiO_2 nanoparticles by graphene nanoflakes; the EDS spectra (Fig. 2d) revealed the presence of C, Ti, O, and N constituents. Furthermore, the prepared powders well poly-crystalline nature with no amorphous domains were exposed in the magnified TEM images and the selected area electron diffraction (SAED) pattern of the representative samples in Fig. 2S b, c, and d of the supplementary information, which is essential prerequisite for improved photocatalytic efficiency.

X-ray photoelectron spectroscopy (XPS) investigation was performed to explore TiO_2-graphene-doped N configuration. The elements, Ti, O, C, and N, were confirmed by examining the survey spectrum (Fig. 3a), the data based on three points showed that the atomic percentages of these elements were 24.1, 53.8, 17.9, and 4.2 at. %, respectively, in the representative $N_{0.06}$-GT powder calcined at 600 °C. Further, to probe the variation in the chemical states, the XPS core energy level spectra of C 1s, Ti 2p, O 1s, and N 1s were measured. In C 1s spectrum (Fig. 3b), the chemical states of C element were as follow: (1) C–C with binding energy of 284.6 eV corresponds to both adventitious carbon from the XPS instrument and to sp^2 hybridized carbon (Zhao et al. 2012). The peaks for N-sp^2 C and N-sp^3 C with the binding energies of 285.5 eV and 286.3 eV were due to the N atom substituting the C atom in graphene, defects, or adsorbed on graphene (Wang et al. 2013; Wei et al. 2009). The peak at binding energy of 288.8 eV represents C-O/O-C = O due to combination of O atom in TiO_2 and C atom of graphene, indicating the chemical intimate contact of graphene with TiO_2 (Ren et al. 2007). The Ti $2p^{3/2}$ and $2p^{1/2}$ were positioned at binding energies of 258.9 eV and 464.9 eV, respectively, in the Ti 2p core level XPS spectrum (Fig. 3c), which is consistent with the value of Ti^{4+} in TiO_2. Additionally,

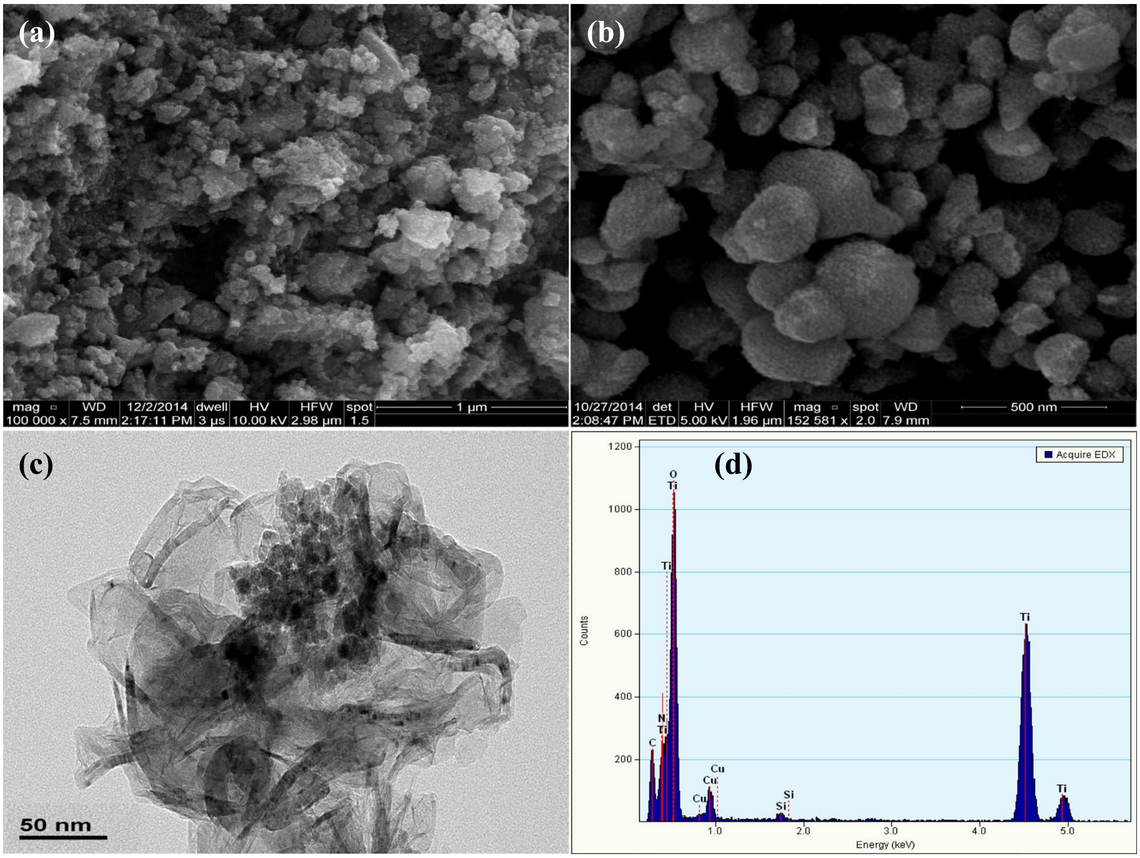

Fig. 2 Microscopy micrographs of the calcined materials; SEM images of **a** T and **b** $N_{0.06}$-GT, **c** HR-TEM image of $N_{0.06}$-GT, and **d** HR-TEM–EDX spectrum of the representative $N_{0.06}$-GT sample

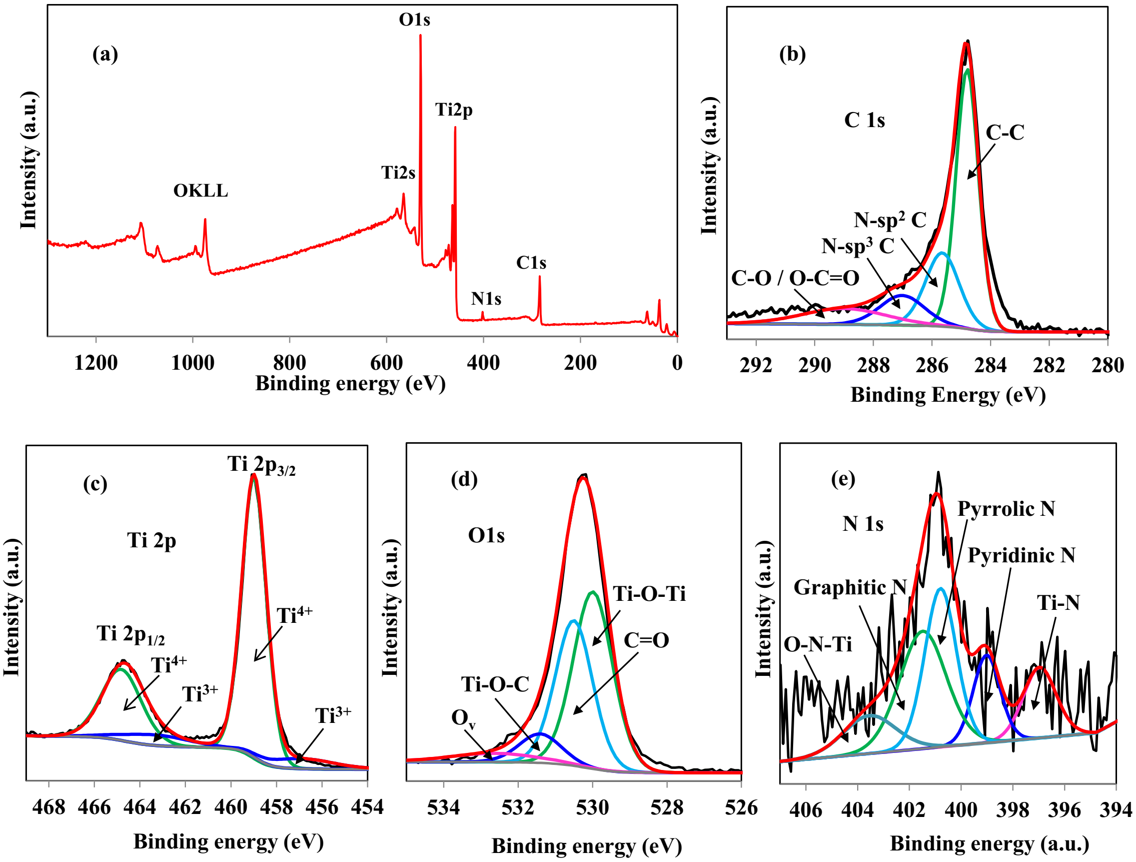

Fig. 3 XPS analysis of the calcined $N_{0.06}$-GT nano-hybrid: **a** survey spectrum; high-resolution spectra of **b** C 1s, **c** Ti 2p, **d** O 1s, and **e** N 1s, respectively

the reduced Ti^{3+} state in TiO_2 was assigned to the binding energy values at 457.8 eV and 463.8 eV.

In the core level XPS spectrum of O 1s (Fig. 3d), on deconvolution, four speaks were observed, Ti–O-Ti peak at 529.8 eV, C = O peak at 530.4 eV, Ti–O-C peak at 531.3 eV, and oxygen vacancy (O_v) peak at 532.2 eV (Liu et al. 2020). The spectrum N 1s core level (Fig. 3e) can be divided into five peaks which corresponds to Ti-N peak at 396.8 eV (Asahi et al. 2001) illustrating the substitution of dopant in titania lattice, the peak at 401.3 eV corresponds to the graphitic N implying that N atoms replace the C atoms in the inner graphene layers (Wei et al. 2009), and the peaks at 398.8 eV and 400.6 eV represent the pyridinic and pyrrolic N, respectively. According to published reports, pyridinic N is electrochemically active nitrogen, because it gives lone pair electrons for conjugation with p-conjugated rings. Pyrolic N is known to possess a sp^2-hybridized graphitic structure and is responsible to enhance the catalytic action of carbon in electron transfer reactions and generate electron-donor attributes to boost graphene electrical conductivity (Fan et al. 2013). The peak at 403.9 eV was ascribed to oxidized nitrogen and or to the O-N-Ti linkages. It is very interesting to note that all nitrogen forms (graphitic-, pyridinic-, pyrrolic-, and oxidized-like nitrogen) served as catalytically active site for oxygen reduction reaction (ORR) (Lee et al. 2017). Moreover, these findings support the successful N chemical doping in both titania and graphene.

The Kubulka-Munk (K-M) approach was utilized to estimate the band gap values of the as-prepared samples, as shown in Table 1. This method translates the diffuse reflectance measurements into equivalent absorption coefficient (α): $\alpha = (1\text{-}R)^2/2R$. To produce Tauc plots ($(\alpha h\upsilon)^{0.5}$ versus photon energy ($h\upsilon$), see Fig. 4a), a tangent line was stretched from the liner portion of the curve to the $h\upsilon$ x-axis at E_g, the value associated with this point of intersection was taken as the indirect band gap value of the final material. Compared to pure anatase TiO_2, the nanocomposite (N-GT) showed red shift towards the longer wavelength, attributed to the N doping and the chemical bonding between TiO_2 and graphene. The incorporation of N atoms into titania crystal lattice alters the electronic band structure causing the formation of a new N 2p impurity energy level above the O 2p valence band. This phenomenon causes the optical absorption to move into the visible light range and narrows the TiO_2 band gap. In addition, the cooperative effect of graphene and titania (Ti–O-C bond) is also beneficial for

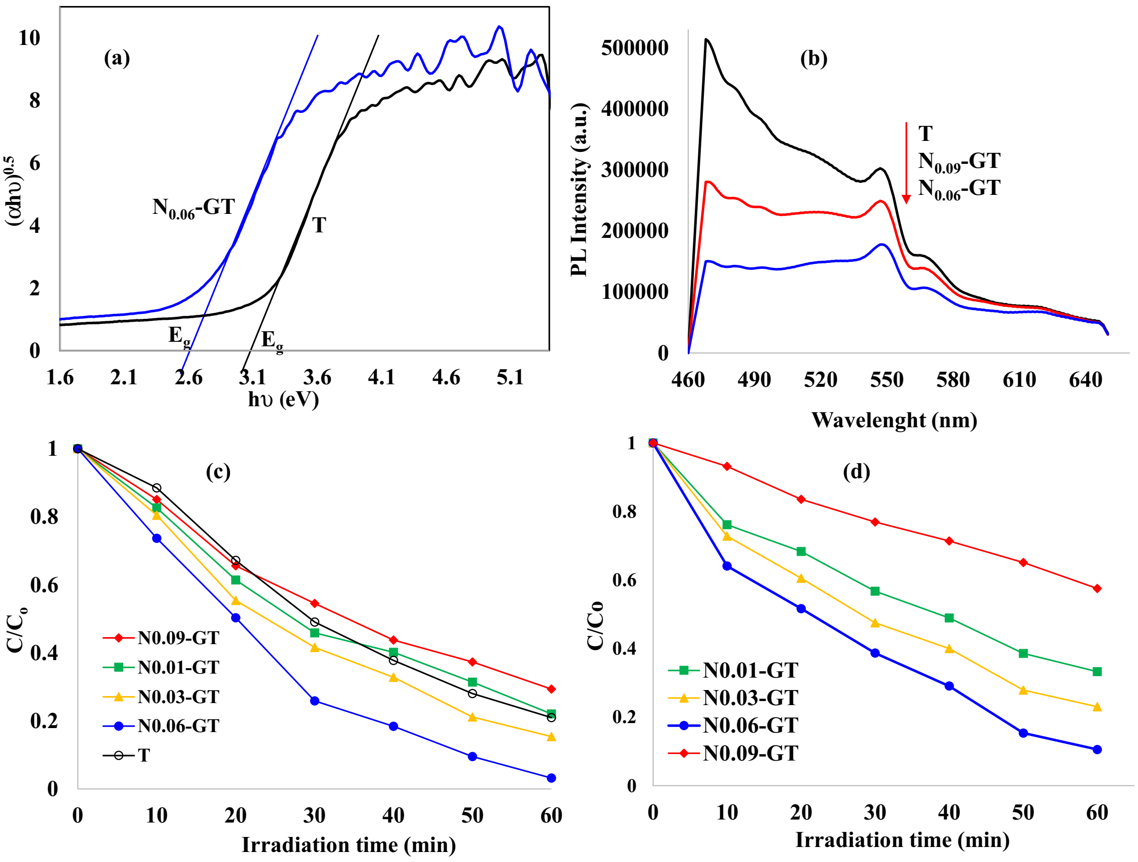

Fig. 4 **a** UV-DRS spectra of T and $N_{0.06}$-GT; **b** PL spectra of T, $N_{0.09}$-GT, and $N_{0.06}$-GT; photocatalytic test of the prepared samples for **c** MB under UV irradiations and **d** SMX under visible light; all the powders were calcined at 600 °C

increasing visible light absorption; as reported, the graphene unpaired π-electron interaction with Ti atoms can stimulate band edge shift and the ultimate narrowing in the band gap of GT (Khan et al. 2018). In summary, the red shift of N-GT absorption edge could be credited to the chemical bonding among the N dopant, titania, and graphene as witnessed from the XPS analysis in addition to the minor presence of O_v defects and Ti^{3+} species.

Photoluminescence is produced on illuminating a photocatalyst with light irradiation; photons are released as a result of recombination of charge (e^-/h^+) carriers. Therefore, photoluminescence (PL) spectra analysis is often used to evaluate e^-/h^+ recombination efficiency in semiconductor particles. As shown in Fig. 4b, the PL intensity drastically decreases for the nanohybrids (N-GT) compared to pure TiO_2 (T), indicating low recombination rate of photoinduced e^-/h^+ pairs and the effective separation and charge carrier transportation within the modified material. The addition of dopant (N) and graphene (G), which function as electron carriers and charge transfer with the TiO_2, can successfully retard the recombination rate. The peaks detected at 550 cm^{-1} and 570 cm^{-1} are associated to the partially reduced titanium ions, surface defects, and oxygen vacancies (Kawai et al. 2012). Moreover, excess dopant content beyond the optimum amount reduces the effective component of photo e^-/h^+ pairs, and at the same time, the photoinduced charge carriers can use the resulting defect states as recombination center and augments the PL intensity increase, thus affecting the photocatalyst activity performance.

Photocatalytic activity

To investigate the ultraviolet (UV) and visible (Vis) light photocatalytic activities of the as-prepared control and nanohybrid materials, degradation tests (each experiment repeated three times) were conducted for the model pollutants in water, methylene blue (MB under UV light), and sulfamethoxazole (SMX, under Vis. light). In earlier works, we have demonstrated that the concentration of the selected pollutant molecule did not change in the blank experiments (UV photolysis (60 min) and visible photolysis (30 min)) containing no photocatalyst. This means that photocatalyst is necessary for the cleavage of the pollutant molecules. Dark tests were performed prior to the activity studies to determine the maximum amount of the pollutant's species adsorbed on the photocatalyst surface. It was demonstrated that in comparison to other synthesized materials, $N_{0.06}$-GT nanohybrid exhibits both enhanced dark MB/SMX adsorption (Table 2) and UV–Vis photocatalytic degradation (Fig. 4c, d). It is necessary to mention here that the determined pH of the point zero charge (pH_{pzc}) of control TiO_2 is 6.1, while for the prepared composite material, the pHpzc value is lower (in range of 5.7–5.8), because nitrogen atoms were substitutionally introduced into oxygen site of TiO_2 lattice. The composite surface has a net negative charge at photocatalytic solution pH above the pHpzc value (Falletta et al. 2023). Since, MB is a cationic dye and pKa value of SMX is 5.0; therefore, the composite surface easily adsorbed enhanced amount of pollutant, and it is expected that higher decomposition rate will be observed. In the UV tests, $N_{0.06}$-GT materials decompose ≈ 98.4% MB compared to pure TiO_2 (60.0%); likewise, under Vis Light, the SMX degradation was ≈ 90.0%. This is obvious that pure TiO_2 is not appropriate for visible light photocatalysis because of its wide band gap, which limits its activity to the UV. The observed photocatalytic trends were for UV light $N_{0.06}$-GT > $N_{0.03}$-GT ≈ $N_{0.09}$-GT > $N_{0.01}$-GT > T and for Vis. light $N_{0.06}$-GT > $N_{0.03}$-GT > $N_{0.01}$-GT ≈ $N_{0.09}$-GT. Since all the photocatalytic materials have comparable crystallinity, phase structure (mainly anatase with minor brookite phase), meso-porosity, and same graphene content, the variation in activity performance can be explained as a function of specific surface area via increased pollutant adsorption, band gap, surface hydroxyl groups, composite homogeneity, decreased electron–hole recombination rate, and dopant concentration.

This is obvious that photocatalysis occur at the surface, the higher BET surface area results in increased pollutant adsorption, while the meso-porous structure enables the diffusion of parent and intermediate pollutant species in and outside the photocatalyst particles. FTIR studies discloses the hybrid materials possess higher degree of hydroxyl group ($N_{0.06}$-GT > $N_{0.03}$-GT > $N_{0.01}$-GT ≈ T > $N_{0.09}$-GT as visualized from the wide trough depth in the region 2860–3400 cm^{-1}); adsorbed water molecules combinedly will promote higher hydroxyl radical ($OH^{\bullet}$) concentration on reaction with photoinduced holes (h^{+}s). Narrowed band gap results in enhanced photon absorption from the UV–Vis region that causes greater number of electron–hole (e^{-}/h^{+}) pair formation necessary for the process redox reactions. SEM analysis presented that the composite samples are uniform and densely ball like packed, as such the contact points between titania and graphene increases, which is beneficial for improved activity. The increased separation between charge carriers and their diffusion to the active site to participate in the decomposition reaction is the key performance indicator factors for enhanced activity. XPS study reveals the presence of defect states (O_v and Ti^{3+}), substitution of N atoms in TiO_2 lattice for impurity level generation, chemical bonding of N atoms in graphene layers, and the anchoring of TiO_2 on graphene nanoflakes, jointly results in enhanced tapping and transport of electrons from the TiO_2 particle (CB, greater electron density area) to the newly formed interface between TiO_2 and graphene, then deeper into the graphene nanoflakes to be consumed in the decomposition reactions.

Moreover, the UV–Vis photocatalytic tests also displayed that the additional increase in the dopant amount beyond the optimum level (0.06 mol% in this case) resulted in a drastic decrease in the pollutant decomposition. This means that excess N atoms may act as charge carrier's recombination centers or in effect some of the increased oxygen vacancies (due to charge compensation) sites become the centers for e^{-}/h^{+} recombination. This is also possible that higher content of dopant in the nanocomposite increases the opacity and light shielding effect, as a result will cause the decrease in light reaching the photocatalyst surface, which produced e^{-}/h^{+} pairs and subsequence radical species, in effect decrease the photocatalytic efficiency of the produced material. In conclusion, the increased photocatalytic activity of the nanohybrid ($N_{0.06}$-GT) is further explained by proposing a mechanism via ROS (reactive oxidizing species) tests as follows.

Table 2 Relative adsorption of MB and SMX in the dark on the as-synthesized material surface before starting the photocatalyst experiments

Prepared material	MB adsorption (Q_{MB})$^{\phi}$ in the dark for UV experiments (mg g^{-1})	SMX adsorption (Q_{MB})$^{\phi}$ in the dark for visible experiments (mg g^{-1})
T	0.9	1.2
$N_{0.01}$-GT	1.3	1.7
$N_{0.03}$-GT	1.7	2.2
$N_{0.06}$-GT	2.4	2.8
$N_{0.09}$-GT	2.1	2.3

$^{\phi}Q=((C_o\text{-}C_e) * V)/W$, where Q (mg g^{-1}) is the quantity of pollutant molecules adsorbed per unit surface of the as-prepared material at adsorption equilibrium, C_o (mg L^{-1}) is the initial concentration, and C_e (mg L^{-1}) is the equilibrium concentration of the pollutant, V (L) is the solution volume, and W (g) is the adsorbent weight

Assessment of radical scavenger and photocatalyst reusability test

The decomposition of pollutant species in the advanced oxidation process of photocatalysis is possible due to the production of reactive oxidizing species (ROS) such as hydroxyl radicals (OH$^\bullet$), super oxide anion species ($O_2^{\bullet -}$), singlet oxygen (O^1), and hydrogen peroxide (H_2O_2) beside the photogenerated holes (h^+s). To investigate which of these ROS are responsible for the increased activity, experiments were performed in the presence of various sacrificial agents comprising tert-butanol (tBuOH, scavenge OH$^\bullet$ radicals), 1,4 benzoquinone (BQ, to annihilate $O_2^{\bullet -}$ species), catalase (catalyzes the H_2O_2 dismutation), azide (N_3^-, consume O^1 species), and potassium iodide (KI, scavenge photoinduced h^+), utilizing the same protocols outlined in our published study (Khan et al. 2017). At our experimental settings, the calculated percent (%) breakdown of MB molecules under UV light in the presence of most active nanomaterial ($N_{0.06}$-GT) was 78, 65, 42, 26, and 9% with tBuOH, BQ, catalase, KI, and N_3^-, respectively; similarly, the trend followed for the degradation of SMX under Vis light was 72, 70.4, 37, 33, and 6% with tBuOH, BQ, catalase, KI, and N_3^-, respectively (Fig. 5a, b). These results imply that primarily OH$^\bullet$ and $O_2^{\bullet -}$ followed by H_2O_2 and h^+s were liable for the degradation of the model pollutants, while the singlet oxygen has no discernible effect on the pollutant degradation process. An experiment was also performed by purging inert nitrogen (N_2) gas during the photocatalytic redox process to evaluate the role of dissolved oxygen (d-O_2); the result showed (Fig. 5c) that d-O_2 is crucial to be available for process redox reactions. To further establish the central role of the mobile hydroxyl radicals, the PL intensity of the produced strongly fluorescent 7-hydroxycoumarine is followed at the maximum 460 nm under the visible excitation at 320 nm (Khan et al. 2019). 7-Hydroxycoumarine is produced from the reaction between the poorly fluorescent molecule of coumarin (antioxidant) and OH$^\bullet$ in aqueous solution. Figure 4 d shows that the sample $N_{0.06}$-GT produces considerable number of hydroxyl radicals in comparison to pure TiO_2, which agrees with the FTIR study exhibiting a wide and deep trough for the OH^- surface functional group

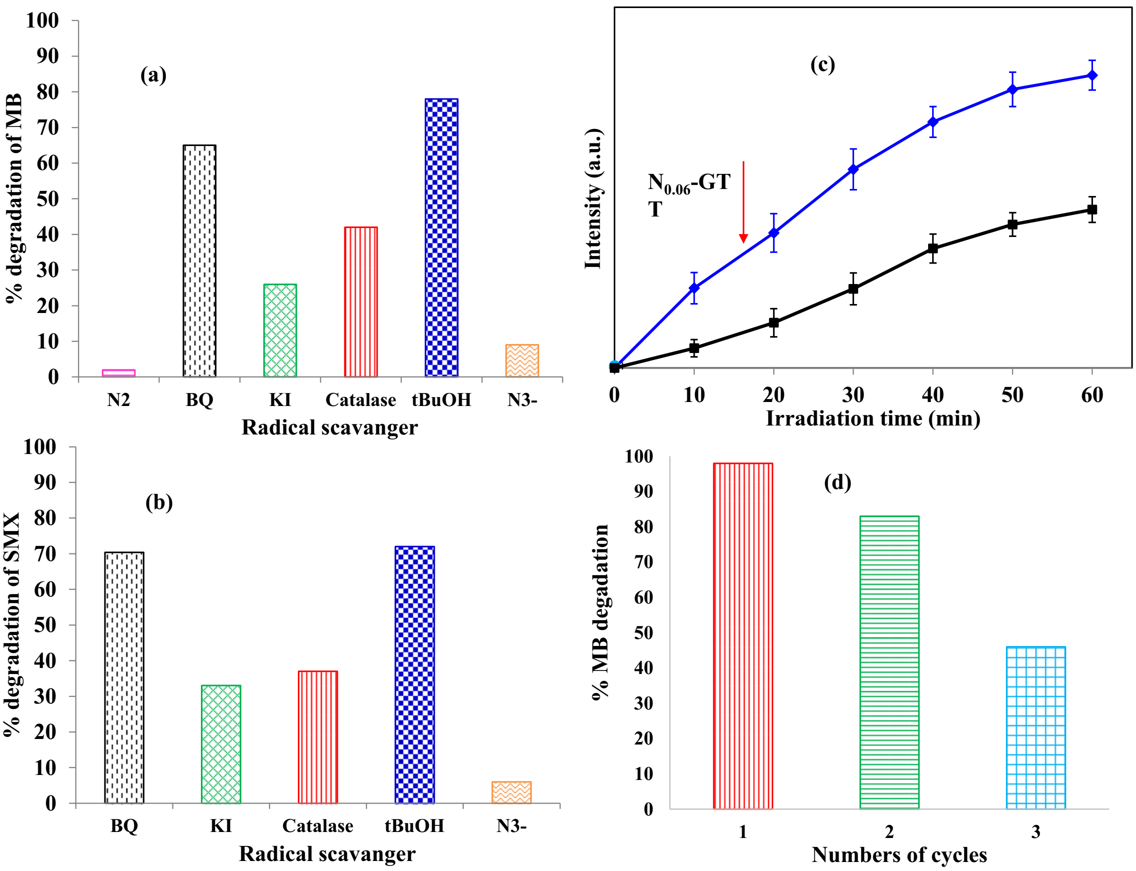

Fig. 5 **a** Degradation of MB with different scavenger and nitrogen (absence of dissolved oxygen) under UV light, **b** degradation of SMX with different scavenger under visible light, **c** change in PL intensity of the highly fluorescent 7-hydroxycoumarine under UV illumination with the calcined representative photocatalysts (T and $N_{0.06}$-GT), and **d** reusability and recyclability of $N_{0.06}$-GT hybrid material against MB degradation under UV irradiation

and the sharp peak for adsorbed water. In addition, the narrowed band gap of 2.60 eV is responsible for more photon absorption in the longer wavelength, thus generating more h$^+$ species which were mainly consumed in the reaction with hydroxyl group to produce hydroxyl radicals.

The photocatalyst (N$_{0.06}$-GT) recyclability and reusability were examined to decompose 6 mg L^{-1} of MB under UV irradiations for three repeated cycles, and the results were depicted in Fig. 5d. At the end of each activity test, the photocatalyst material was separated by filtration, washed two to three times with DI water, dried at 80 °C overnight, and reused for fresh MB solution. The material displayed very promising reusability results; for the first two consecutive cycles, the photocatalyst material activity was greater than 80%. Later in the third cycle, a sharp decline in powder activity was recorded; the reason may be deposition of the undecomposed MB in the porous structure of the photocatalyst and material loss during the cleaning (filtration and washing) and collection process.

Proposed mechanism

Based on the recorded characterization and activity results, a probable mechanism for the UV–Vis photocatalytic process over N-GT nanohybrid is illustrated in Fig. 6. On light irradiation, electron (e$^-$) is promoted to the conduction band (CB), while a hole (h$^+$) is left in the valance band (VB) of N-doped TiO$_2$. The electrons in CB react with the externally supplied oxygen to generate mainly the superoxide anions (O$_2^{\bullet-}$), also can generate hydrogen peroxide via the reaction mentioned as Eq. 1. The hydrogen peroxide on further reaction with photoinduced electrons produces hydroxyl ions and hydroxyl radicals (Eq. 2). There is also the possibility that hydrogen peroxide reacts with VB holes to produce superoxide anions (Eq. 3). The produced radical species are then used in the degradation process. The VB holes are consumed in the production of hydroxyl radicals via the reaction mentioned as Eq. 4; the h$^+$s may also be used directly for the degradation of pollutant molecules (Eq. 5). The N 2p level electrons positioned above the VB maximum (O 2p) and reducing the TiO$_2$ band gap can be excited under light illumination to the CB level, followed by transferring to the NG flakes via the Ti–O-C bands due to low fermi level of NG compared to NT (Eq. 6) (Qian et al. 2014). In the meantime, the incremental h$^+$s in NG is diffused to the NT VB, which can further segregate e$^-$/h$^+$ and retard the recombination process, leading to increased degradation rate. As a result, e^-_s are grouped on the NG flakes, whereas h$^+$s is clustered on NT surface. XPS studies revealed that NT and NG are in intimate contact with each other; the d-orbital of NT and the π-orbital of graphene match incredibly well in energy levels, forming a d-π electron orbital overlap because of chemical bond interaction that can have a synergistic impact (Zhao et al. 2012). When UV–Vis light is absorbed by NT, the energized e$^-$s are migrated from the NT CB d-orbital into the NG π-orbital and are then freely transported along the excellent conducting channel network of graphene, then finally diffuse to the surface to react with adsorbed oxygen and water to crop hydroxyl radicals, which would decayed pollutant species via the reactions displayed as Eq. 7. This said process allows charge separation, stabilization, and delayed recombination.

Reactions

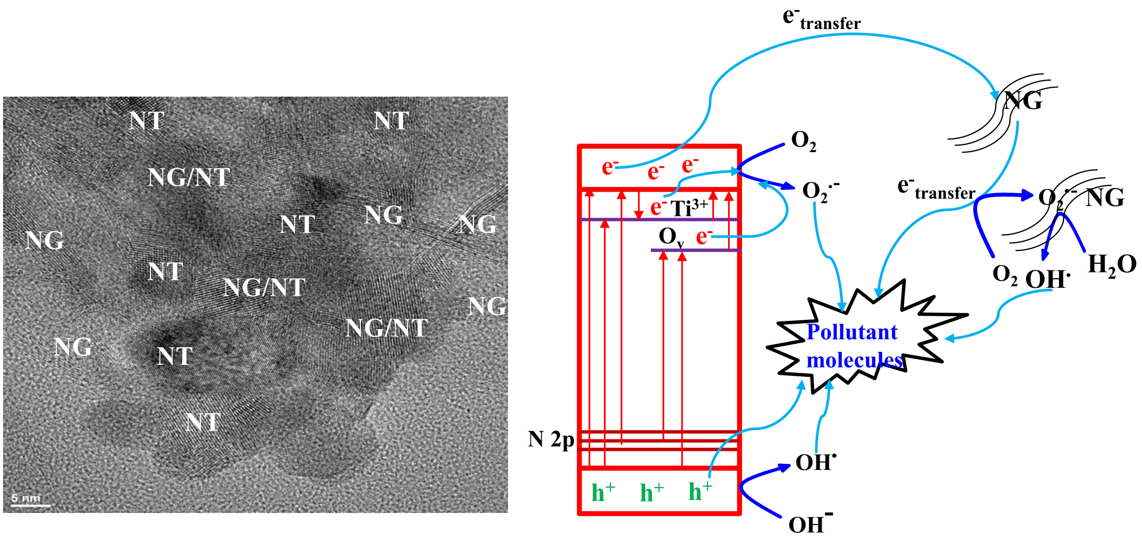

Fig. 6 Proposed mechanism showing the transfer pathways of the photogenerated charge carriers and various oxidizing species contributing to the degradation of model pollutant molecules

$$O_2^{\bullet -} + H^+ + 2e^- \rightarrow H_2O_2 \tag{1}$$

$$H_2O_2 + e^- \rightarrow OH^- + OH^\bullet \tag{2}$$

$$H_2O_2 + h_{VB}^+ \rightarrow O_2^{\bullet -} + H^+ \tag{3}$$

$$h^+ + OH^- \rightarrow OH^\bullet \tag{4}$$

$$h^+ + \text{pollutant molecules} \rightarrow \text{degraded products} \tag{5}$$

$$h\nu + NT \rightarrow e_{CB}^- + e_{VB}^+ \rightarrow NG(e^-) + h^+ \tag{6}$$

$$NG\ (e^-) + O_{2ads} \rightarrow O_2^{\bullet -} + NG \overset{H_2O}{\rightarrow} OH^\bullet + NG; OH^\bullet + \text{ pollutant species } \rightarrow \text{degraded products} \tag{7}$$

Moreover, the adsorption capacity of NT bound to NG notably improved because of increased active sites accessible on the surface of NG. Since adsorbed oxygen on surface active site of NG followed by $OH^\bullet$ radical's formation as said earlier. To put it briefly, the system containing NT bonded to NG produces more $OH^\bullet$ radicals than the one containing NT alone as a photocatalyst. Furthermore, via π-π conjugation between SMX/MB and the aromatic frameworks of the NG, SMX/MB species can diffuse from solution to the surface of the material and be adsorbed with offset face-to-face orientation. As a result, the SMX/MB adsorptivity on NG increases in relation to that of SMX/MB on pure TiO_2 (Qian et al. 2014). Hence, as a photocatalyst, NT/NG (N-GT) is more efficient than T alone in the photodecomposition of SMX/MB.

The 3d state of Ti^{3+} below that of CB at ~ 1.2 eV bordering to the oxygen vacancy (O_v) can also act as e^-s trapping zone consequently enhancing the charge segregation and its diffusion to reaction sites (Wang et al. 2009). The trapped electrons in these states can also be excited to the NT CB level; also, Ti^{3+} and O_v act as sites which actively aid in chemisorbed oxygen species formation during photocatalytic water purification (Padmanabhan et al. 2021). However, it is to be noted that because of excess dopant content, the h^+s in N 2p states in the band gap created by interstitial N dopant are greatly localized and, thus, possess a weak mobility, on interaction with the 3d states of Ti^{3+} acts as a recombination center and badly effect the material activity (Wang et al. 2009).

In conclusion, N doping in TiO_2 induces the N 2p states which results in enhanced production of charge carrier due to increased photons absorption in the UV–Vis region, in addition produces O_v states in TiO_2 due to charge compensation that acts as charge trapping sites. The N ions in graphene accelerate the electron transport via improved charge separation. The chemical anchoring of NT on NG further improves the band gap, also accelerate the separation of photoinduced e^-/h^+ charge pairs, and the presence of mesopores

Table 3 Photocatalytic degradation of MB and SMX at different experimental conditions using other hybrid TiO_2 composites in comparison to present work

Material	Synthesis method	Light source	Pollutant amount degraded	Ref
$N\text{-}TiO_2$	Sol–gel	UV emitting LED strip	MB 52% in 2.5 h	Vaiano et al. (2015)
TiO_2@r-GO (15%)	Hydrothermal	Solar light (Osram's Ultra Vitalux lamp)	MB 98% in 2 h	Kocijan et al. (2021)
$N\text{-}TiO_2/C$	Templation	Mercury lamp	MB 77% in 0.84 h	Yao et al. (2019)
TiO_2/GO (8%)	Liquid phase deposition	Sunlight	MB 98% in 4 h	Khan et al. (2019)
$N\text{-}TiO_{2nanowire}/N\text{-}GO$	Hydrothermal	Xenon lamp with 420 nm cut-off filter	MB 90% in 3 h	Liu et al. (2016)
$N\text{-}G/TiO_2$	Hydrothermal	Xenon lamp	MB 80% in 1 h	Li et al. (2015)
N,S codoped $TiO_2/r\text{-}GO_{(5\%)}$	Hydrothermal	Tungsten (500 W) lamp	MB 64% in 1 h	Brindha and Sivakumar (2017)
r-GO-TiO_2/sodium alginate, [TiO_2 – Sigma-Aldrich]	Hydrothermal	UV-A	SMX 99% in 0.75 h	Nawaz et al. (2020)
Degussa P-25 TiO_2	-	UV light	SMX 40% in 0.5 h	Nasuhoglu et al. (2011)
Ag-TiO_2/N-GO	Hydrothermal	8 W white LED's	SMX 83% in 6 h	Urda et al. (2022)
N-TG	Sol–gel	UV and visible light	MB 98% in 1 h (UV light) SMX 92% in 1 h (visible light)	This work

(as a result of porous structure) can provide additional active sites for adsorption and favors the enhanced production of ROS species ($O_2^{\bullet -}$, $OH^{\bullet}$) leading to excellent photocatalytic efficiency of the composite material. Moreover, Table 3 illustrates a comparative literature review related to the current work; however, exact comparison will not be possible due to variation in photocatalyst synthesis method and procedure, use of different precursors and operating conditions, different concentration of chemicals, and irradiation time and source used during the photocatalytic reactions, etc.

Conclusion

It was demonstrated that N-doped TiO_2 chemically anchored on N-doped graphene nanoflakes; i.e., N-GT nanohybrids can be constructed through a facile and friendly sol–gel method. The successful substitution of N doping both in TiO_2 crystal lattice and into the skeleton of graphene nanoflakes was shown by the results of Raman spectroscopy, UV–Vis absorption spectra, and XPS spectroscopy. Under both visible and ultraviolet light illumination, the N-GT composite showed improved photocatalytic activity in comparison to pure TiO_2. The maximum photodecomposition of MB and SMX can be ascribed to the combined effect of narrowed band gap due to N doping. Increased specific surface area via enhanced pollutant adsorptivity on the nano-hybrid photocatalyst surface and efficient e^-/h^+ pairs separation due to graphene two-dimensional planar structure and the potential for enhanced π-π interaction between nanostructure material and organic compound. Finally, the author believes that this study opens new possibilities into the investigation of very attractive N-doped TiO_2-graphene hybrids and supports their possible practical applications in environmental remediation, production of value-added products, energy production, and storage issues. Moreover, the stated photocatalyst synthesis process is very simple, economical, and feasible to carried on large scale; this study also opens new avenues to explore in situ nitrogen doping with coupled TiO_2 and GO (graphene oxide) and or r-GO (reduced graphene oxide). Both GO and r-GO synthesis process is simple and can be carried out on large scale as compared to pure graphene used in this study.

Supplementary Information The online version contains supplementary material available at https://doi.org/10.1007/s11356-024-34114-y.

Acknowledgements The author gratefully acknowledges the Department of Chemical Engineering, King Faisal University, Kingdom of Saudi Arabia (KSA), for supporting this study. We would especially like to express our gratitude to the Departments of Chemistry and Chemical Engineering (McGill University, Montreal), as well as Department of Chemistry (University of Montreal), for granting us permission to use their laboratory chemical reagents and analytical tools, including the FTIR, UV-Vis DRS, PL, and Raman, for the photocatalyst activity tests and characterization.

Author contribution Hayat Khan is the sole author of this paper. All the work (study conception, design and methodology, material preparation and experimentations, data collection and analysis, manuscript planning, writing and editing) is performed by the author itself.

Data Availability Not applicable.

Declarations

Ethics approval Ethical approval is not required for this research.

Consent to participate Not applicable.

Consent for publication The author has checked the manuscript and has agreed to give the consent for the publication of this work and or identifiable details, which can include photograph(s) and/or details within the text to be published in the Journal Environmental Science and Pollution Research.

Competing interests The author declares no competing interests.

References

Asahi R, Morikawa T, Irie H, Ohwaki T (2014) Nitrogen-doped titanium dioxide as visible-light-sensitive photocatalyst: designs, developments, and prospects. Chem Rev 114(19):9824–9852

Asahi R, Morikawa T, Ohwaki T, Aoki K, Taga Y (2001) Visible-light photocatalysis in nitrogen-doped titanium oxides. Science 293(5528):269–271

Brindha A, Sivakumar T (2017) Visible active N, S co-doped TiO_2/graphene photocatalysts for the degradation of hazardous dyes. J Photochem Photobiol, A 340:146–156

Catania F, Marras E, Giorcelli M, Jagdale P, Lavagna L, Tagliaferro A, Bartoli M (2021) A review on recent advancements of graphene and graphene-related materials in biological applications, Appl Sci

Chandra S, Jagdale P, Medha I, Tiwari AK, Bartoli M, Nino AD, Olivito F (2021) Biochar-supported TiO_2-based nanocomposites for the photocatalytic degradation of sulfamethoxazole in water—A review, Toxics

Chang DW, Baek JB (2016) Nitrogen-doped graphene for photocatalytic hydrogen generation. Chemistry–An Asian Journal 11(8):1125–1137

Chen X, Qiao L, Zhao R, Wu J, Gao J, Li L, Chen J, Wang W, Galloni MG, Scesa FM, Chen Z, Falletta E (2023) Recent advances in photocatalysis on cement-based materials. J Environ Chem Eng 11(2):109416

Cheng X, Yu X, Xing Z, Yang L (2016) Synthesis and characterization of N-doped TiO_2 and its enhanced visible-light photocatalytic activity. Arab J Chem 9:S1706–S1711

Divyasri YV, Reddy NL, Lee K, Sakar M, Rao VN, Venkatramu V, Shankar MV, Reddy NCG (2021) Optimization of N doping in TiO_2 nanotubes for the enhanced solar light mediated photocatalytic H_2 production and dye degradation. Environ Pollut 269:116170

Falletta E, Galloni MG, Mila N, Roslan MNB, Ghani NA, Cerrato G, Giordana A, Magni M, Spriano S, Boffito DC, Bianchi CL (2023) Fast and efficient piezo-photocatalytic mineralization of Ibuprofen by BiOBr nanosheets under solar light irradiation. ACS Photonics 10(11):3929–3943

Fan W, Xia YY, Tjiu WW, Pallathadka PK, He C, Liu T (2013) Nitrogen-doped graphene hollow nanospheres as novel electrode materials for supercapacitor applications. J Power Sources 243:973–981

Fu Y, Gao G, Zhi J (2019) Electrochemical synthesis of multicolor fluorescent N-doped graphene quantum dots as a ferric ion sensor and their application in bioimaging. J Mater Chem B 7(9):1494–1502

Inagaki M (2000) New carbons — control of structure and functions. Elsevier Science, The Netherlands

Kawai T, Kishimoto Y, Kifune K (2012) Photoluminescence studies of nitrogen-doped TiO_2 powders prepared by annealing with urea. Phil Mag 92(33):4088–4097

Khalid NR, Ahmed E, Hong Z, Zhang Y, Ahmad M (2012) Nitrogen doped TiO_2 nanoparticles decorated on graphene sheets for photocatalysis applications. Curr Appl Phys 12(6):1485–1492

Khan H, Jiang Z, Berk D (2018) Molybdenum doped graphene/TiO_2 hybrid photocatalyst for UV/visible photocatalytic applications. Sol Energy 162:420–430

Khan H, Swati IK, Younas M, Ullah A (2017) Chelated nitrogen-sulphur-codoped TiO_2: synthesis, characterization, mechanistic, and UV/visible photocatalytic studies. Int J Photoenergy 2017:7268641

Khan SA, Arshad Z, Shahid S, Arshad I, Rizwan K, Sher M, Fatima U (2019) Synthesis of TiO_2/graphene oxide nanocomposites for their enhanced photocatalytic activity against methylene blue dye and ciprofloxacin. Compos B Eng 175:107120

Kocijan M, Curkovic L, Ljubas D, Muzina K, Bacic I, Radosevic T, Podlogar M, Bdikin I, Irurueta GO, Hortiguela MJ, Goncalves G (2021) Graphene-based TiO_2 nanocomposite for photocatalytic degradation of dyes in aqueous solution under solar-like radiation, Appl Sci

Lee YJ, Kim NY, Shin DY, Park HY, Lee SS, Joon SK, Lim DH, Bong KW, Son JG, Kim JY (2017) Nitrogen-doped graphene-wrapped iron nanofragments for high-performance oxygen reduction electrocatalysts. J Nanopart Res 19(3):98

Li H, Liu B, Wang Y, Li H, Yin S, Ma X, Li Y, Wang X, Wu Q (2015) N-doped graphene/TiO_2 nanocomposite with enhanced photocatalytic activity. J Nanosci Nanotechnol 15(9):7141–7145

Liu C, Zhang L, Liu R, Gao Z, Yang X, Tu Z, Yang F, Ye Z, Cui L, Xu C, Li Y (2016) Hydrothermal synthesis of N-doped TiO_2 nanowires and N-doped graphene heterostructures with enhanced photocatalytic properties. J Alloy Compd 656:24–32

Liu J, Chen KY, Wang J, Du M, Gao ZY, Song CX (2020) Preparation and photocatalytic properties of N-doped graphene/TiO_2 composites. J Chem 2020:2928189

Maouche C, Zhou Y, Peng J, Wang S, Sun X, Rahman N, Yongphet P, Liu Q, Yang J (2020) A 3D nitrogen-doped graphene aerogel for enhanced visible-light photocatalytic pollutant degradation and hydrogen evolution. RSC Adv 10(21):12423–12431

Mou Z, Wu Y, Sun J, Yang P, Du Y, Lu C (2014) TiO_2 nanoparticles-functionalized N-doped graphene with superior interfacial contact and enhanced charge separation for photocatalytic hydrogen generation. ACS Appl Mater Interfaces 6(16):13798–13806

Nasuhoglu D, Yargeau V, Berk D (2011) Photo-removal of sulfamethoxazole (SMX) by photolytic and photocatalytic processes in a batch reactor under UV-C radiation (λ_{max}=254nm). J Hazard Mater 186(1):67–75

Nawaz M, Khan AA, Hussain A, Jang J, Jung HY, Lee DS (2020) Reduced graphene oxide−TiO_2/sodium alginate 3-dimensional structure aerogel for enhanced photocatalytic degradation of ibuprofen and sulfamethoxazole. Chemosphere 261:127702

Oladoye PO, Ajiboye TO, Omotola EO, Oyewola OJ (2022) Methylene blue dye: Toxicity and potential elimination technology from wastewater. Results Eng 16:100678

Padmanabhan NT, Thomas N, Louis J, Mathew DT, Ganguly P, John H, Pillai SC (2021) Graphene coupled TiO_2 photocatalysts for environmental applications: a review. Chemosphere 271:129506

Praveen P, Viruthagiri G, Mugundan S, Shanmugam N (2013) Structural, optical and morphological analyses of pristine titanium dioxide nanoparticles-synthesized via sol-gel route. Spectrochim Acta Part A Mol Biomol Spectrosc 117:622–629

Pristavita R, Meunier JC, Berk D (2011) Carbon nano-flakes produced by an inductively coupled thermal plasma system for catalyst applications. Plasma Chem Plasma Process 31(2):393–403

Qian W, Greaney PA, Fowler S, Chiu SK, Goforth AM, Jiao J (2014) Low-temperature nitrogen doping in ammonia solution for production of N-doped TiO_2-hybridized graphene as a highly efficient photocatalyst for water treatment. ACS Sustain Chem Eng 2(7):1802–1810

Ren W, Ai Z, Jia F, Zhang L, Fan X, Zou Z (2007) Low temperature preparation and visible light photocatalytic activity of mesoporous carbon-doped crystalline TiO_2. Appl Catal B 69(3):138–144

Ruta V, Sivo A, Bonetti L, Bajada MA, Vile G (2022) Structural effects of metal single-atom catalysts for enhanced photocatalytic degradation of gemfibrozil. ACS Appl Nano Mater 5(10):14520–14528

Sinhmar A, Setia H, Kumar V, Sobti A, Toor AP (2020) Enhanced photocatalytic activity of nickel and nitrogen codoped TiO_2 under sunlight. Environ Technol Innov 18:100658

Smirniotis PG, Boningari T, Inturi SNR (2018) Single-step synthesis of N-doped TiO_2 by flame aerosol method and the effect of synthesis parameters. Aerosol Sci Technol 52(8):913–922

Sordello F, Zeb G, Hu K, Calza P, Minero C, Szkopek T, Cerruti M (2014) Tuning TiO_2 nanoparticle morphology in graphene–TiO_2 hybrids by graphene surface modification. Nanoscale 6(12):6710–6719

Tang H, Wang M, Ju T, Dai Y, Wang M, Ma Y, Zheng G (2022) Nitrogen-doped TiO_2/graphene composites synthesized via the vapour-thermal method. J Wuhan Univ Technol-Mater. Sci. Ed. 37(6), 1105–1113

Urda A, Radu T, Socaci C, Avram VF, Cosma D, Rosu MC, Coros M, Pruneanu S, Pogacean F (2022) Evaluation of N-doped graphene role in the visible-light driven photodegradation of sulfamethoxazole by a TiO_2-silver-graphene composite. J Photochem Photobiol, A 425:113701

Vaiano V, Sacco O, Sannino D, Ciambelli P (2015) Nanostructured N-doped TiO_2 coated on glass spheres for the photocatalytic removal of organic dyes under UV or visible light irradiation. Appl Catal B 170–171:153–161

Wang G, Xing W, Zhuo S (2013) Nitrogen-doped graphene as low-cost counter electrode for high-efficiency dye-sensitized solar cells. Electrochim Acta 92:269–275

Wang J, Tafen DN, Lewis JP, Hong Z, Manivannan A, Zhi M, Li M, Wu N (2009) Origin of photocatalytic activity of nitrogen-doped TiO_2 nanobelts. J Am Chem Soc 131(34):12290–12297

Wei D, Liu Y, Wang Y, Zhang H, Huang L, Yu G (2009) Synthesis of N-doped graphene by chemical vapor deposition and Its electrical properties. Nano Lett 9(5):1752–1758

Wen Y, Ding H, Shan Y (2011) Preparation and visible light photocatalytic activity of Ag/TiO_2/graphene nanocomposite. Nanoscale 3(10):4411–4417

Xu H, Ma L, Jin Z (2018) Nitrogen-doped graphene: synthesis, characterizations and energy applications. J Energy Chem 27(1):146–160

Xu X, Yuan T, Zhou Y, Li Y, Lu J, Tian X, Wang D, Wang J (2014) Facile synthesis of boron and nitrogen-doped graphene as efficient electrocatalyst for the oxygen reduction reaction in alkaline media. Int J Hydrogen Energy 39(28):16043–16052

Yang Q, Ma Y, Chen F, Yao F, Sun J, Wang S, Yi K, Hou L, Li X, Wang D (2019) Recent advances in photo-activated sulfate radical-advanced oxidation process (SR-AOP) for refractory organic pollutants removal in water. Chem Eng J 378:122149

Yao L, Wang H, Zhang Y, Wang S, Liu X (2019) Fabrication of N doped TiO_2/C nanocomposites with hierarchical porous structure and high photocatalytic activity. Microporous Mesoporous Mater 288:109604

Yao Z, Dr YJ, Lei G, Mietek J, Shi ZQ (2013) Two-step boron and nitrogen doping in graphene for enhanced synergistic catalysis. Angewandte Zuschriften 125(11):3192–3198

Zhao D, Sheng G, Chen C, Wang X (2012) Enhanced photocatalytic degradation of methylene blue under visible irradiation on graphene@TiO_2 dyade structure. Appl Catal B 111–112:303–308

Zhou K, Zhu Y, Yang X, Jiang X, Li C (2011) Preparation of graphene–TiO_2 composites with enhanced photocatalytic activity. New J Chem 35(2):353–359